Two mirror X-ray pulse split and delay instrument for femtosecond time resolved investigations at the LCLS free electron laser facility

Nora Berrah,[1,*] Li Fang,[2] Brendan F Murphy,[3] Edwin Kukk,[4] Timur Y. Osipov,[5] Ryan Coffee,[5] Ken R Ferguson,[5] Hui Xiong,[1] Jean-Charles Castagna,[5] Vlad S Petrovic,[6] Sebastian Carron Montero,[5] and John D. Bozek[5]

[1]Physics Department, University of Connecticut, Storrs, 06269, USA
[2]Center for High Energy Density Science, University of Texas at Austin, Austin, 78712 USA
[3]Physics Department, Western Michigan University, Kalamazoo, 49008, USA
[4]Department of Physics and Astronomy, University of Turku, FI-20014, Turku, Finland
[5]LCLS, SLAC National Laboratory, Menlo Park, 94025, USA
[6]PULSE Institute, SLAC National Laboratory, Menlo Park, 94025, USA
[*]Nora.Berrah@uconn.edu

Abstract: We built a two-mirror based X-ray split and delay (XRSD) device for soft X-rays at the Linac Coherent Light Source free electron laser facility. The instrument is based on an edge-polished mirror design covering an energy range of 250 eV-1800 eV and producing a delay between the two split pulses variable up to 400 femtoseconds with a sub-100 attosecond resolution. We present experimental and simulation results regarding molecular dissociation dynamics in CH_3I and CO probed by the XRSD device. We observed ion kinetic energy and branching ratio dependence on the delay times which were reliably produced by the XRSD instrument.

OCIS codes: (020.0020) Atomic and molecular physics; (320.0320) Ultrafast optics; (340.0340) X-ray optics.

References and links

1. W. Ackermann, G. Asova, V. Ayvazyan, A. Azima, N. Baboi, J. Bähr, V. Balandin, B. Beutner, A. Brandt, A. Bolzmann, R. Brinkmann, O. I. Brovko, M. Castellano, P. Castro, L. Catani, E. Chiadroni, S. Choroba, A. Cianchi, J. T. Costello, D. Cubaynes, J. Dardis, W. Decking, H. Delsim-Hashemi, A. Delserieys, G. Di Pirro, M. Dohlus, S. Düsterer, A. Eckhardt, H. T. Edwards, B. Faatz, J. Feldhaus, K. Flöttmann, J. Frisch, L. Fröhlich, T. Garvey, U. Gensch, Ch. Gerth, M. Görler, N. Golubeva, H.-J. Grabosch, M. Grecki, O. Grimm, K. Hacker, U. Hahn, J. H. Han, K. Honkavaara, T. Hott, M. Hüning, Y. Ivanisenko, E. Jaeschke, W. Jalmuzna, T. Jezynski, R. Kammering, V. Katalev, K. Kavanagh, E. T. Kennedy, S. Khodyachykh, K. Klose, V. Kocharyan, M. Körfer, M. Kollewe, W. Koprek, S. Korepanov, D. Kostin, M. Krassilnikov, G. Kube, M. Kuhlmann, C. L. S. Lewis, L. Lilje, T. Limberg, D. Lipka, F. Löhl, H. Luna, M. Luong, M. Martins, M. Meyer, P. Michelato, V. Miltchev, W. D. Möller, L. Monaco, W. F. O. Müller, O. Napieralski, O. Napoly, P. Nicolosi, D. Nölle, T. Nuñez, A. Oppelt, C. Pagani, R. Paparella, N. Pchalek, J. Pedregosa-Gutierrez, B. Petersen, B. Petrosyan, G. Petrosyan, L. Petrosyan, J. Pflüger, E. Plönjes, L. Poletto, K. Pozniak, E. Prat, D. Proch, P. Pucyk, P. Radcliffe, H. Redlin, K. Rehlich, M. Richter, M. Roehrs, J. Roensch, R. Romaniuk, M. Ross, J. Rossbach, V. Rybnikov, M. Sachwitz, E. L. Saldin, W. Sandner, H. Schlarb, B. Schmidt, M. Schmitz, P. Schmüser, J. R. Schneider, E. A. Schneidmiller, S. Schnepp, S. Schreiber, M. Seidel, D. Sertore, A. V. Shabunov, C. Simon, S. Simrock, E. Sombrowski, A. A. Sorokin, P. Spanknebel, R. Spesyvtsev, L. Staykov, B. Steffen, F. Stephan, F. Stulle, H. Thom, K. Tiedtke, M. Tischer, S. Toleikis, R. Treusch, D. Trines, I. Tsakov, E. Vogel, T. Weiland, H. Weise, M. Wellhöfer, M. Wendt, I. Will, A. Winter, K. Wittenburg, W. Wurth, P. Yeates, M. V. Yurkov, I. Zagorodnov, and K. Zapfe, "Operation of a free-electron laser from the extreme ultraviolet to the water window," Nat. Photonics **1**(6), 336–342 (2007).
2. P. Emma, R. Akre, J. Arthur, R. Bionta, C. Bostedt, J. Bozek, A. Brachmann, P. Bucksbaum, R. Coffee, F.-J. Decker, Y. Ding, D. Dowell, S. Edstrom, A. Fisher, J. Frisch, S. Gilevich, J. Hastings, G. Hays, Ph. Hering, Z. Huang, R. Iverson, H. Loos, M. Messerschmidt, A. Miahnahri, S. Moeller, H.-D. Nuhn, G. Pile, D. Ratner, J. Rzepiela, D. Schultz, T. Smith, P. Stefan, H. Tompkins, J. Turner, J. Welch, W. White, J. Wu, G. Yocky, and J.

#262243 Received 1 Apr 2016; revised 16 May 2016; accepted 16 May 2016; published 20 May 2016

Galayda, "First lasing and operation of an ångstrom-wavelength free-electron laser," Nat. Photonics **4**(9), 641–647 (2010).
3. E. Allaria, R. Appio, L. Badano, W. A. Barletta, S. Bassanese, S. G. Biedron, A. Borga, E. Busetto, D. Castronovo, P. Cinquegrana, S. Cleva, D. Cocco, M. Cornacchia, P. Craievich, I. Cudin, G. D'Auria, M. Dal Forno, M. B. Danailov, R. De Monte, G. De Ninno, P. Delgiusto, A. Demidovich, S. Di Mitri, B. Diviacco, A. Fabris, R. Fabris, W. Fawley, M. Ferianis, E. Ferrari, S. Ferry, L. Froehlich, P. Furlan, G. Gaio, F. Gelmetti, L. Giannessi, M. Giannini, R. Gobessi, R. Ivanov, E. Karantzoulis, M. Lonza, A. Lutman, B. Mahieu, M. Milloch, S. V. Milton, M. Musardo, I. Nikolov, S. Noe, F. Parmigiani, G. Penco, M. Petronio, L. Pivetta, M. Predonzani, F. Rossi, L. Rumiz, A. Salom, C. Scafuri, C. Serpico, P. Sigalotti, S. Spampinati, C. Spezzani, M. Svandrlik, C. Svetina, S. Tazzari, M. Trovo, R. Umer, A. Vascotto, M. Veronese, R. Visintini, M. Zaccaria, D. Zangrando, and M. Zangrando, "Highly coherent and stable pulses from the FERMI seeded free-electron laser in the extreme ultraviolet," Nat. Photonics **6**(10), 699–704 (2012).
4. T. Ishikawa, H. Aoyagi, T. Asaka, Y. Asano, N. Azumi, T. Bizen, H. Ego, K. Fukami, T. Fukui, Y. Furukawa, S. Goto, H. Hanaki, T. Hara, T. Hasegawa, T. Hatsui, A. Higashiya, T. Hirono, N. Hosoda, M. Ishii, T. Inagaki, Y. Inubushi, T. Itoga, Y. Joti, M. Kago, T. Kameshima, H. Kimura, Y. Kirihara, A. Kiyomichi, T. Kobayashi, C. Kondo, T. Kudo, H. Maesaka, X. M. Maréchal, T. Masuda, S. Matsubara, T. Matsumoto, T. Matsushita, S. Matsui, M. Nagasono, N. Nariyama, H. Ohashi, T. Ohata, T. Ohshima, S. Ono, Y. Otake, C. Saji, T. Sakurai, T. Sato, K. Sawada, T. Seike, K. Shirasawa, T. Sugimoto, S. Suzuki, S. Takahashi, H. Takebe, K. Takeshita, K. Tamasaku, H. Tanaka, R. Tanaka, T. Tanaka, T. Togashi, K. Togawa, A. Tokuhisa, H. Tomizawa, K. Tono, S. Wu, M. Yabashi, M. Yamaga, A. Yamashita, K. Yanagida, C. Zhang, T. Shintake, H. Kitamura, and N. Kumagai, "A compact X-ray free-electron laser emitting in the sub-ångström region," Nat. Photonics **6**(8), 540–544 (2012).
5. F. Sorgenfrei, W. F. Schlotter, T. Beeck, M. Nagasono, S. Gieschen, H. Meyer, A. Föhlisch, M. Beye, and W. Wurth, "The extreme ultraviolet split and femtosecond delay unit at the plane grating monochromator beamline PG2 at FLASH," Rev. Sci. Instrum. **81**(4), 043107 (2010).
6. J. M. Glownia, J. Cryan, J. Andreasson, A. Belkacem, N. Berrah, C. I. Blaga, C. Bostedt, J. Bozek, L. F. DiMauro, L. Fang, J. Frisch, O. Gessner, M. Gühr, J. Hajdu, M. P. Hertlein, M. Hoener, G. Huang, O. Kornilov, J. P. Marangos, A. M. March, B. K. McFarland, H. Merdji, V. S. Petrovic, C. Raman, D. Ray, D. A. Reis, M. Trigo, J. L. White, W. White, R. Wilcox, L. Young, R. N. Coffee, and P. H. Bucksbaum, "Time-resolved pump-probe experiments at the LCLS," Opt. Express **18**(17), 17620–17630 (2010).
7. J. P. Cryan, J. M. Glownia, J. Andreasson, A. Belkacem, N. Berrah, C. I. Blaga, C. Bostedt, J. Bozek, C. Buth, L. F. DiMauro, L. Fang, O. Gessner, M. Guehr, J. Hajdu, M. P. Hertlein, M. Hoener, O. Kornilov, J. P. Marangos, A. M. March, B. K. McFarland, H. Merdji, V. S. Petrović, C. Raman, D. Ray, D. Reis, F. Tarantelli, M. Trigo, J. L. White, W. White, L. Young, P. H. Bucksbaum, and R. N. Coffee, "Auger electron angular distribution of double core-hole states in the molecular reference frame," Phys. Rev. Lett. **105**(8), 083004 (2010).
8. Y. Ding, F. J. Decker, P. Emma, C. Feng, C. Field, J. Frisch, Z. Huang, J. Krzywinski, H. Loos, J. Welch, J. Wu, F. Zhou, and F. Zhou, "Femtosecond x-ray pulse characterization in free-electron lasers using a cross-correlation technique," Phys. Rev. Lett. **109**(25), 254802 (2012).
9. M. Woestmann, R. Mitzner, T. Noll, S. Roling, B. Siemer, F. Siewert, S. Eppenhoff, F. Wahlert, and H. Zacharias, "The XUV split-and-delay unit at beamline BL2 at FLASH," J. Phys. At. Mol. Opt. Phys. **46**(16), 164005 (2013).
10. Y. H. Jiang, A. Rudenko, O. Herrwerth, L. Foucar, M. Kurka, K. U. Kühnel, M. Lezius, M. F. Kling, J. van Tilborg, A. Belkacem, K. Ueda, S. Düsterer, R. Treusch, C. D. Schröter, R. Moshammer, and J. Ullrich, "Ultrafast extreme ultraviolet induced isomerization of acetylene cations," Phys. Rev. Lett. **105**(26), 263002 (2010).
11. C. E. Liekhus-Schmaltz, I. Tenney, T. Osipov, A. Sanchez-Gonzalez, N. Berrah, R. Boll, C. Bomme, C. Bostedt, J. D. Bozek, S. Carron, R. Coffee, J. Devin, B. Erk, K. R. Ferguson, R. W. Field, L. Foucar, L. J. Frasinski, J. M. Glownia, M. Gühr, A. Kamalov, J. Krzywinski, H. Li, J. P. Marangos, T. J. Martinez, B. K. McFarland, S. Miyabe, B. Murphy, A. Natan, D. Rolles, A. Rudenko, M. Siano, E. R. Simpson, L. Spector, M. Swiggers, D. Walke, S. Wang, T. Weber, P. H. Bucksbaum, and V. S. Petrovic, "Ultrafast isomerization initiated by X-ray core ionization," Nat. Commun. **6**, 8199 (2015).
12. C. Castagna, B. Murphy, J. Bozek, and N. Berrah, "X-ray split and delay for soft x-rays at LCLS," J. Phys. Conf. Ser. **425**(15), 152021 (2013).
13. B. Erk, R. Boll, S. Trippel, D. Anielski, L. Foucar, B. Rudek, S. W. Epp, R. Coffee, S. Carron, S. Schorb, K. R. Ferguson, M. Swiggers, J. D. Bozek, M. Simon, T. Marchenko, J. Küpper, I. Schlichting, J. Ullrich, C. Bostedt, D. Rolles, and A. Rudenko, "Imaging charge transfer in iodomethane upon x-ray photoabsorption," Science **345**(6194), 288–291 (2014).
14. K. Motomura, E. Kukk, H. Fukuzawa, S. Wada, K. Nagaya, S. Ohmura, S. Mondal, T. Tachibana, Y. Ito, R. Koga, T. Sakai, K. Matsunami, A. Rudenko, C. Nicolas, X. J. Liu, C. Miron, Y. Zhang, Y. Jiang, J. Chen, M. Anand, D. E. Kim, K. Tono, M. Yabashi, M. Yao, and K. Ueda, "Charge and nuclear dynamics induced by deep inner-shell multiphoton ionization of CH_3I molecules by intense x-ray free-electron laser pulses," J. Phys. Chem. Lett. **6**(15), 2944–2949 (2015).
15. M. Hoener, L. Fang, O. Kornilov, O. Gessner, S. T. Pratt, M. Gühr, E. P. Kanter, C. Blaga, C. Bostedt, J. D. Bozek, P. H. Bucksbaum, C. Buth, M. Chen, R. Coffee, J. Cryan, L. Dimauro, M. Glownia, E. Hosler, E. Kukk, S. R. Leone, B. McFarland, M. Messerschmidt, B. Murphy, V. Petrovic, D. Rolles, and N. Berrah, "Ultraintense

#262243 Received 1 Apr 2016; revised 16 May 2016; accepted 16 May 2016; published 20 May 2016

x-ray induced ionization, dissociation, and frustrated absorption in molecular nitrogen," Phys. Rev. Lett. **104**(25), 253002 (2010).
16. L. Young, E. P. Kanter, B. Krässig, Y. Li, A. M. March, S. T. Pratt, R. Santra, S. H. Southworth, N. Rohringer, L. F. Dimauro, G. Doumy, C. A. Roedig, N. Berrah, L. Fang, M. Hoener, P. H. Bucksbaum, J. P. Cryan, S. Ghimire, J. M. Glownia, D. A. Reis, J. D. Bozek, C. Bostedt, and M. Messerschmidt, "Femtosecond electronic response of atoms to ultra-intense X-rays," Nature **466**(7302), 56–61 (2010).
17. L. Fang, D. Rolles, A. Rudenko, V. Petrovich, C. Bostedt, J. D. Bozek, P. Buckbaum, and N. Berrah, "Probing ultrafast electronic and molecular dynamics with free electron lasers," J. Phys. At. Mol. Opt. Phys. **47**(12), 124006 (2014).
18. K. R. Ferguson, M. Bucher, J. D. Bozek, S. Carron, J. C. Castagna, R. Coffee, G. I. Curiel, M. Holmes, J. Krzywinski, M. Messerschmidt, M. Minitti, A. Mitra, S. Moeller, P. Noonan, T. Osipov, S. Schorb, M. Swiggers, A. Wallace, J. Yin, and C. Bostedt, "The atomic, molecular, and optical science instrument at the linac coherent light source," J. Synchrotron Radiat. **22**(3), 492–497 (2015).

1. Introduction

Free electron lasers around the world with unprecedented vuv or x-ray peak power such as FLASH in Hamburg, Germany [1], the Linac Coherent Light source (LCLS) at SLAC National Laboratory in the United States [2], FERMI@ Elletra in Trieste, Italy [3] and the Spring-8 SACLA in Japan [4], make possible novel femtosecond dynamic investigations in atoms, molecules, liquids and solids as well as in biological specimens. These dynamic experiments rely on pump-probe techniques similar to the ones used with table-top lasers. The first mirror-based instrument that allowed pump-probe experiment in the extreme uv range was built and commissioned at the FLASH FEL [5].

Several methods to study molecular dynamics using pump-probe techniques have been used at the LCLS [6,7] since 2009 when the facility opened to users. These schemes were complemented by a novel accelerator-based method in 2012 whereby two x-ray pulses separated in time were produced by means of a slotted foil [8]. The independent production of FEL radiation from two portions of the electron bunch that pass through the slots in the foil leads to two ultrafast x-ray pulses. In this case, however, the FEL self-amplified spontaneous emission (SASE) pulses cannot provide assurances that both pulses will have consistent amplitudes or pulse energies in each of the two pulses. Nevertheless, this scheme works well for several types of experiments.

Another scheme which can be used for the study of molecular dynamics is to split the incoming x-ray pulse into two parts and delay one of them. This method has been used in the vacuum ultraviolet (vuv) wavelength regime using multiple mirrors at the FLASH vuv/soft x-ray FEL [5, 9, 10]. One of the devices was built on the plane grating monochromator beamline PG2 at the FLASH facility. This tool is comprised of eight mirrors; four mirrors which split, steer and recombine the incoming photon beam into two beams, while the other four mirrors provide the delay by means of a movable mounting, changing the optical path length. The strength of the eight mirrors device is that it can achieve a wide range of delays which in this case are between –5.1 and + 5.1 ps with an uncertainty in the temporal accuracy of 210 as [5]. Another device generates xuv-pump-probe pulses, using a split-mirror [10] which was installed at beamline BL 3 of FLASH. This device consists of a spherical multilayer mirror that is cut into two identical half-mirrors with a reflectivity of 40%, optimized at 38 eV. Only one half-mirror is movable along the FEL beam axis by means of a high-precision stage to determine the time delay for a range of ± 2.5 ps at a resolution of about 1 fs [10]. A more recent split and delay unit (SDU) at FLASH consists of extreme ultraviolet (xuv) pump–xuv probe implemented for beamline BL2. This is the second SDU at FLASH which is located at beamline BL2. Although the design of this device is different compared to the one at beamline PG2 [5], it is also an eight mirrors system as in [5]. This new SDU tool divides geometrically the beam into two paths which can be delayed from –3 to + 15 ps with respect to each other. Almost the whole FLASH photon energy range is covered by this new SDU [9].

#262243 Received 1 Apr 2016; revised 16 May 2016; accepted 16 May 2016; published 20 May 2016

We have designed, built and successfully utilized an x-ray split and delay (XRSD) device that consists of two mirrors. The advantage of this design is that it is compact, removable, relatively low cost and simpler than previously described split and delay devices [5,9] as well as transportable to other beamlines. Its limitation is that it does not extend into the picosecond range, but achieves the maximum of 400 fs delays. This XRSD instrument is located immediately after the Kirkpatrick-Baez mirrors situated at the Atomic and Molecular (AMO) beamline. This system can also be used at the soft x-ray (SXR) beamline. The two x-ray pulses are separated by up to 400 fs with a sub-fs time resolution and the device functions over the full soft x-ray photon energy range of LCLS which is 250-1800 eV. Although the soft x-ray beamline reaches 2000 eV, the photon energy's upper limit is due to the KB mirror coating, which results in a cut-off of reflectivity at 1800 eV. This device has been used successfully in an x-ray probe x-ray pump experiment regarding ultrafast isomerization of acetylene initiated by x-ray core ionization [11].

2. Design and working principle of the XRSD instrument

The XRSD device consists of two plane mirrors that intercept the x-ray beam between the Kirkpatrick-Baez (KB) focusing optics and the experimental chamber [12]. The KB optics focus the beam at the interaction region of the chamber. The XRSD device is situated between the focus of the beam and the KB optics, so that the distance between the KB optics and the XRSD device is 1m while the distance between the XRSD device and the chamber is 1.5 m. In such a layout, the photon density on the XRSD optics is only about a factor of four higher than on the KB mirrors and is not more damaging for the XRSD device than for the KB mirrors. Furthermore, the XRSD optics are not coated in order to avoid radiation damage.

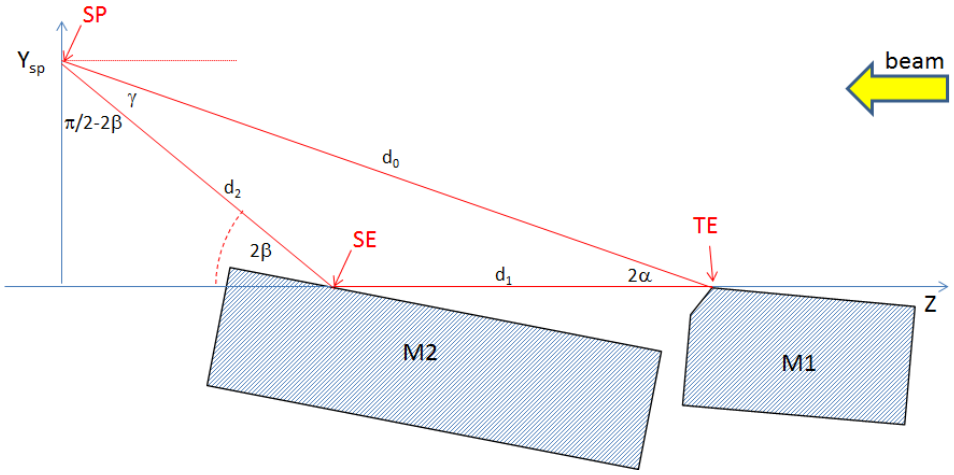

Fig. 1. The principle of the XRSD device. SP: sample position (focal spot with two beams overlapped). SE: shadow's edge position (back edge of the beam on M2, which is formed by the cut off by M1). TE: trailing edge (front edge of the beam on M1, which is formed by the mirror edge). α, β are the tilt angles of M_1 and M_2.d_0: distance from the trailing edge TE on M_1 to SP. d_1: distance TE and SE. d_2: distance from SE on M_2 to SP.

Figure 1 shows the schematic of the XRSD device. As shown in Fig. 1, the vertical portion below the highest point of mirror 1 (M_1) (the trailing edge TE) is reflected by M1 and the part of the beam passing over TE illuminates mirror 2 (M_2) after passing over a shadowed region, starting from the shadow's edge (SE) position. The intercept angles of the mirrors are adjustable together with the vertical positions of their optical surfaces, which allows control of the intensity ratio and overlap of the split beam.

The beam focused by the KB mirrors upstream is thus split into two portions following different optical paths starting from the trailing edge (TE) position. The first beam reaches the

#262243 Received 1 Apr 2016; revised 16 May 2016; accepted 16 May 2016; published 20 May 2016

sample position (SP) along d_0 and is intercepted by the second beam following the path d_1, d_2 as shown in Fig. 1. The time delay Δt between the pulses is:

$$\Delta t = \frac{(d_1 + d_2 - d_0)}{c} \tag{1}$$

where c is the speed of light. From the vertical positions of the SP by M_1 and M_2, one finds the path d_2 in terms of d_0 and the angles α, and β in the following way:

$$\begin{aligned} M_1: &\quad y_{foc} = d_0 \sin 2\alpha \\ M_2: &\quad y_{foc} = d_2 \sin 2\beta \end{aligned} \quad \Rightarrow \quad d_2 = \frac{d_0 \sin 2\alpha}{\sin 2\beta} \tag{2}$$

For a desired delay time Δt, the following relation between the angles and distances is obtained:

$$\beta = \frac{\alpha d_0}{c\Delta t + d_0 - d_1} \tag{3}$$

In order to find d_1, we use the trigonometric relationship and we use Eq. (2) for the path d_2, which allowed us to obtain:

$$d_1 = d_0 \left(\cos 2\alpha - \frac{\sin 2\alpha}{\tan 2\beta} \right) \tag{4}$$

We then plug Eq. (4) into Eq. (3) to obtain the following relationship for the angle β:

$$\beta = \alpha \frac{1}{\frac{c\Delta t}{d_0} + 1 - \cos 2\alpha + \frac{\sin 2\alpha}{\tan 2\beta}} \tag{5}$$

Equation (5) has no exact analytical solution for the angle β as a function of (Δt), but by developing the cosine function into Taylor series, we obtained:

$$\frac{\sin 2\alpha}{\tan 2\beta} = \frac{\sin 2\alpha \cos 2\beta}{\sin 2\beta} \approx \frac{\alpha}{\beta} \cos 2\beta \approx \frac{\alpha}{\beta} \left(1 - \tfrac{1}{2}(2\beta)^2\right) \tag{6}$$

By plugging Eq. (6) into Eq. (5), we obtain the angle β associated with mirror M_2 in terms of the angle and distance, and we obtain α and d_0 associated with mirror M_1:

$$\beta \approx \frac{\frac{c\Delta t}{d_0} + 1 - \cos 2\alpha}{2\alpha} \tag{7}$$

For any desired delay time Δt, one first needs to calculate the tilt angle β of M_2 at the given tilt angle α of M_1 and the distance d_0. The required distance d_1 can then be calculated using Eq. (4). Zero delay is achieved when the two mirror surfaces are coplanar:

$$\beta \approx \frac{1 - \cos 2\alpha}{2\alpha} \approx \frac{1 + 2\alpha^2}{2\alpha} = \alpha \quad \overset{(4)}{\Rightarrow} d_1 = 0 \tag{8}$$

Further simplification of Eq. (7) connecting the pitch angle of the mirrors and the time delay Δt, based on the small angles approximation, gives the following result:

$$\Delta t = 2 d_0 \alpha \Delta\alpha / c \tag{9}$$

#262243 Received 1 Apr 2016; revised 16 May 2016; accepted 16 May 2016; published 20 May 2016

where $\Delta\alpha = \beta - \alpha$.

When comparing to the exact result given by Eq. (5), we found this formula to be accurate to the fourth significant digit in the range of angles and delays possible with the XRSD system.

Moreover, the $\Delta\alpha$ quantity is the exact pitch angle one needs to apply to the mirror 2 with respect to the original 0 fs delay configuration to change the delay, which makes the use of this formula even more practical.

The outline of the compact, practical design is given in Fig. 2 and a more detailed rendering of the 3D model drawing is in Fig. 3. The mirrors are fabricated from uncoated Si and the length of the optical surfaces are 150 mm for M_1 and 400 mm for M_2. A particularly critical design issue was obtaining a clean separation of the beams over the trailing edge TE of M_1; this was achieved by lapping a chamfer in the last step of the overall manufacturing and polishing process. The mirrors are mounted on pivot mounts where the pivot axes are 397 mm lower than the optical surfaces.

The actual control of the mirror motors does not allow for the direct change of the $d_1$parameter but rather the height of the mirror that in turn affects d_1. It is thus more practical to use the following formula that gives this height shift, "h", as a function of the $\Delta\alpha$ established by Eq. (9):

$$h = d_0 \Delta\alpha \tag{10}$$

To take into account the vertical "parasitic motion" of the M2 mirror during the rotation, due to the position of the pivot point, the resulting Eq. (10) can be improved by including one more term as in:

$$h = d_0 \Delta\alpha + R(\Delta\alpha)^2 / 2 \tag{11}$$

Where R is the 397 mm distance from the pivot point to the mirror surface. This second order correction, however, is still less than 1% and only becomes measurable at highest delays.

Another useful result can be obtained by expressing a simplified formula for d_1 in terms of the above directly controllable parameters:

$$d_1 = d_0 \Delta\alpha / (\alpha + \Delta\alpha) \tag{12}$$

Since d_1 is limited by the length of the M2 mirror, inverting Eq. (4) and substituting it into Eq. (9) provides the upper limit on the highest possible delay.

#262243 Received 1 Apr 2016; revised 16 May 2016; accepted 16 May 2016; published 20 May 2016

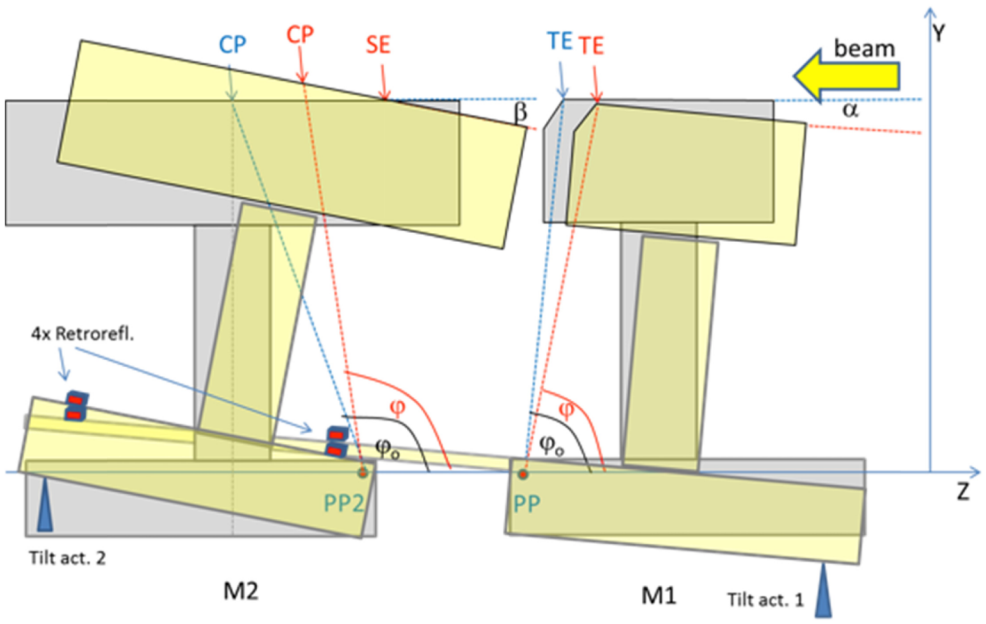

Fig. 2. Outline of the compact design of the XRSD instrument, showing two tilt settings. CP refers to the middle point of the M_2 optical surface.

3. Technical realization of the XRSD instrument

The tilt and vertical position of both M_1 and M_2 can be adjusted independently. Pivoting is achieved by operating on the base of the mounts by two tilt actuators. Both mounts are also equipped with vertical actuators operating on pivot points along the y-direction. In addition, the entire mirror mounting assembly including the actuators can be precision aligned relative to its mounting frame. This alignment is done during the pre-experiment survey and allows to (i) set the XRSD instrument to a specific distance from the sample position (d_0) and (ii) to put both mirrors at a pre-set common tilt angle α_{ch} that then needs to be accounted for in calculating the delay parameters.

The changes in the positions of the mirrors can be read by the encoders of the four actuators. In addition, an even more accurate determination of the relative positions is provided by two Renishaw RLD10-X3DI differential interferometers which measure the distances between two pairs of retroreflectors attached to the two mirror mounts as shown in Figs. 2 and 3. One retroreflector of each pair is mounted directly on the baseplate of M_2 and their opposites are mounted on an extension arm attached to the M_1 mount, extending alongside the M_2 baseplate. Distance measurements from the two pairs thus allow recalculation of the relative heights and angles of the two mirrors.

#262243 Received 1 Apr 2016; revised 16 May 2016; accepted 16 May 2016; published 20 May 2016

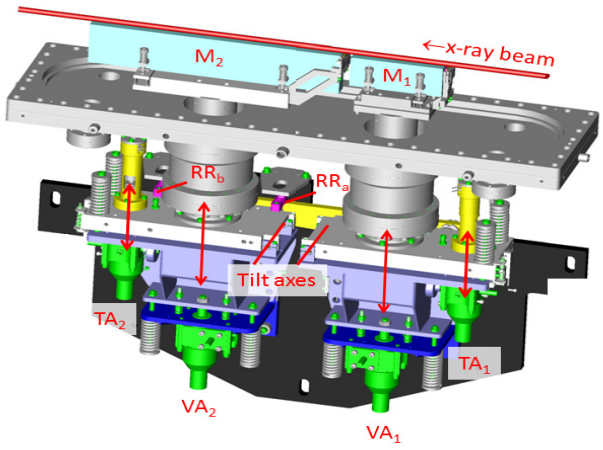

Fig. 3. Rendering of the XRSD device design drawing showing the main alignment features. The frame and the vacuum chamber's top part are removed. TA_n and VA_n (n = 1, 2 for mirror M_1 and M_2 respectively) refer to the tilt and vertical actuators, respectively, and $RR_{a,b}$ mark the two pairs of retroreflectors.

4. Setting delays and verifying motion interdependencies of the XRSD instrument

Prior to the commissioning experiment, the XRSD instrument chamber survey set d_1 to be 1.2495 m and the angle of the mirror mounting assembly at α_{ch} = 11 mrad relative to the incoming x-ray beam axis. It can be shown (see Eqs. (12) and (9)) that at this value of α_{ch} and 400 mm length of M2 the obtainable delay can be greater than 400 fs. During the commissioning of the instrument, the tilt angle of M_1 was left unchanged, no additional tilt was introduced by the actuator, and thus $\alpha = \alpha_{ch}$. Adjustment of the height of M_1 determines the ratio of the flux illuminating the M_1 and M_2 surfaces. During the commissioning of the instrument,TE was positioned at approximately the middle of the beam's vertical profile, splitting the beam into two equal half, as verified by a YAG crystal mounted in front of M_2. Then, M_2 was set to a coplanar position with both roll and height adjusted to give a well-focused single spot at SP from the two reflections. This zero-delay position was then used as a reference for subsequent settings and its actuator encoder as well as interferometer readings were recorded.

For each delay setting, the required values of $\Delta\alpha$ and h were first calculated from Eqs. (9) and (11), using the given $\alpha = \alpha_{ch}$ and d_0. Then the necessary change in the M_2 tilt and M_2 height actuator positions was calculated by referring to the coordinates of the relevant mechanical points. These obtained actuator movements were added to the reference values at the zero-delay settings and then the actuators were operated to run to the desired absolute values. In practice, a worksheet was used, with the desired delay as an input and the final actuator readings as output. At small angles the dependencies are linear and for the particular α and d_0 values they were:

$$\Delta M_2^{tilt}(mm) = 0.00365\,\Delta t(fs)\;;\quad \Delta M_2^{lift}(mm) = -0.01316\,\Delta t(fs)$$

At the new settings, the operator adjusted either one of the M_2 actuators to check for the best overlap of the split beams at SP. High charge states in Argon mass spectrum were used,

#262243 Received 1 Apr 2016; revised 16 May 2016; accepted 16 May 2016; published 20 May 2016

since they are created by multiphoton absorption and thus their relative intensity is very sensitive to the photon density at SP, allowing the determination to find the best overlap of two beams.

The operator-adjusted pairs of ΔM_2^{tilt} *vs.* ΔM_2^{lift} were found for many delay settings and are displayed in Fig. 4, showing two run sequences. The graph demonstrates that the device is mechanically stable and the settings are reproducible – both runs follow closely the same linear curve with the slope of −3.72, which agrees with the calculated value of −3.19 based on mirror positions. The cause of this discrepancy is not yet known. Amongst the possibilities are: the actual distance d_0 was different than assumed (a 5 mm difference accounts for the discrepancy); the encoder readings vs. actual distances need recalibrations; there was an error in the dimensions of the drawing. The graph also shows that for the M_1 tilt angle of 11 mrad, usable delay settings as high as $\Delta t > 200\ fs$ were found. In fact, the upper delay limit is 400 fs for photon energies from 280 eV-1500 eV. The usable delay time drops to 200 fs between 1600 and 1800 eV.

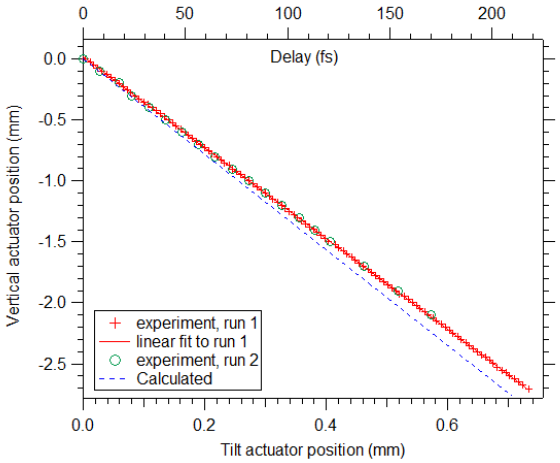

Fig. 4. M_2 actuator positions for overlapping beams at various delays. The zero-delay positions are taken as reference.

5. Experimental results and discussions regarding the XRSD instrument performance

5.1 X-ray pump and probe dissociation of methyl iodide molecules

We used methyl iodide (CH_3I) as the test case molecule for the commissioning of the XRSD device. This molecule has been extensively studied before using XFEL pulses from both LCLS [13] and SACLA [14]. Our experiment showed strong delay-dependent effects that could be represented by a simple model. We recorded the ion time-of-flight (TOF) spectra of the fragments originating from single-molecule targets exposed to the maximum intensity of 1600 eV x-ray pulses of 50 fs duration, varying the delay settings of the XRSD device as shown in Fig. 5. The choice of the photon energy enables a site specific ionization of iodine in the CH_3I molecule, since the iodine atom has a much higher photoionization cross-section than the atoms in the methyl group at this x-ray energy. Also, at the pulse fluences obtainable at the LCLS, sequential multiphoton absorption processes are prevalent. A simplified description of events [13] is 1) Inner shell electrons of the iodine atom in CH_3I are emitted by x-ray ionization, creating positive charge in iodine. 2) Fast charge transfer occurs as electrons from the methyl group fill the vacancies in iodine. 3) Auger cascades multiply the positive charge and are also an efficient mechanism of charge transfer across the molecule. 4) Once the methyl group obtains sufficient positive charge, the molecule undergoes Coulomb

#262243 Received 1 Apr 2016; revised 16 May 2016; accepted 16 May 2016; published 20 May 2016

explosion producing atomic ions. 5) Photoionization and charging up of the atomic iodine continues after the molecular bonds are broken. However, efficient charge transfer from the iodine atom is possible only in the molecular environment.

This ionization scenario results in a wide range of I^{n+}, C^{m+} and H^{+} fragments that can be detected by an ion TOF spectrometer as shown in Fig. 5 spectra. The kinetic energy release (KER) and energies of the individual fragments not only depends on the final charge states of the ions, but also on the *time of the charge creation* with respect to the progress of the molecular fragmentation. Using a single 50 fs pulse, the majority of the charge is created at interatomic distances that are still relatively close to the initial equilibrium ones. Therefore, the conversion of deposited energy into the kinetic energy of the ions by Coulomb repulsion is efficient, resulting in highly energetic fragments.

In a two-pulse scheme, the first pulse duration of 50 fs is long enough so that all molecular bonds can be considered broken by the end of the pulse. Since the number of photons in each pulse is now about 1/4 of that in a single-pulse experiment, the total charge created after the first pulse is, *on average*, also a quarter of that in the single-pulse experiment. Part of this charge is distributed also to the methyl group. The KER that is dependent on the charge state, is significantly lower after the first pulse than in a single pulse experiment.

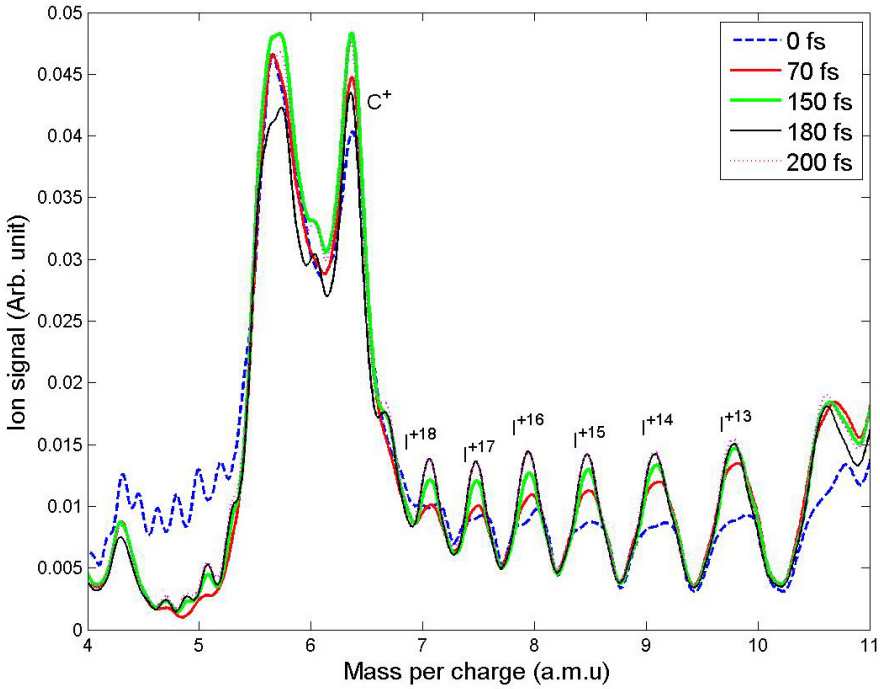

Fig. 5. TOF spectra at various pump-probe delay times. The spectra are normalized to match the dip position for I^{13+}. I^{16+} for comparison of the peak shapes. Data were taken at 1600 eV and a total pulse energy of 1.4 mJ (nominal value measured upstream. At the interaction region, the pulse energy is ~25% of the nominal value, due to optical transport loss [15, 16]).

The second pulse, arriving after the delay ΔT, continues to ionize the iodine atom, which has already separated from the molecular ion. Larger distances mean that (i) the C and H do not obtain additional charge during the second pulse and that (ii) the additional KER due to the increased charge is small compared to the initial KER.

The expectation is thus that the kinetic energy of the fragments should be strongly dependent on the delay times. As an observable effect, Fig. 5 shows clearly the TOF peak's

#262243 Received 1 Apr 2016; revised 16 May 2016; accepted 16 May 2016; published 20 May 2016

different shapes of the ion charge states which are sharper for long delay times (Δt = 150 fs-200 fs) and wider for short delay time (Δt = 70 fs-0 fs). The connection between these changes and the changes in the kinetic energy of the fragments is explained below.

Figure 6 shows peaks in the measured ion TOF spectra of the fragments from the dissociation of CH_3I, induced either by a single 50 fs XFEL pulse or by split pulses with a 200 fs delay. The TOF peak shape of the low charge fragment I_2^+ in Fig. 6(a) is completely insensitive to the introduction of the delay. This is because such low charge states are most likely a result of single photon absorption in either the first or second pulse, effectively reducing the split-pulse (two-pulses) measurement to the single-pulse one. In contrast, the highly charged fragment I^{15+} in Fig. 6(b) has a TOF line shape that is strongly dependent on whether the ionization is by single or split pulse, since it clearly exhibits a much narrower shape with split-pulse ionization. Line widths in this type of ion TOF spectroscopy are indicative of the kinetic energy of the ions: higher initial kinetic energy of the ions tends to alter the ion flight times slightly either increasing or decreasing them (depending upon the initial time-of-flight direction), thus broadening the spectral shapes. This effect can be reproduced quantitatively by Monte-Carlo simulations, tracking the path of the ions through the modeled electric fields of the given spectrometer. Figure 6(c) shows such simulated I^{15+} peak shapes based on the spectrometer's dimensions and voltages used in our experiment. In order to recreate the TOF peak shapes that most closely fit the observations, the ions are randomly created in the Monte-Carlo simulation according to a certain statistical initial kinetic energy distribution; the TOF lineshape is then derived from many individual trajectories and reflects the distribution of the calculated TOFs. The maximum and width of the energy distribution are the adjustable parameters in the simulations, thus allowing us to derive quantitative estimates for the actual observation. In the present simulations, the initial kinetic energies were chosen from a Gaussian distribution (truncated at zero). The best agreement with the single-pulse experiment (red dotted curve in Fig. 6 (b)) was obtained with the distribution having the maximum at 16 eV and the width of 7 eV full width half maximum (FWHM). The split-pulse experiment at 200 fs delay (blue curve in Fig. 6(b)) corresponds to the energy distribution with the maximum at 7 eV and the width of 11 eV. Thus the narrowing of the line shape corresponds to more than double the decrease of the kinetic energy.

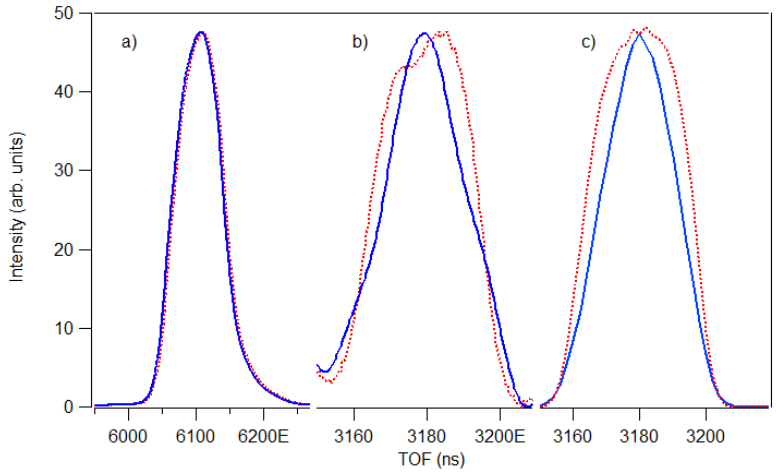

Fig. 6. Ion TOF spectra of CH_3I ionized by 1600 eV, 50 fs pulses. Red dotted curves: zero delay time. Blue solid curves: split pulses with 200 fs delay. a) I^{2+} peak (experimental data), b) I^{15+} peak (experimental data) and c) I^{15+} peak, Monte Carlo simulated. All peaks are normalized to equal height.

#262243 Received 1 Apr 2016; revised 16 May 2016; accepted 16 May 2016; published 20 May 2016

The test experiment demonstrates that the ion KEs of iodine high charge states are indeed sensitive indicators of the second pulse's delay time, as predicted. Long delays, when about 50% of the photons interact with well-separated atomic fragments, create iodine ions with significantly lower energy than at the zero delay, even if the same final charge state is reached. It also appears from the simulation that although the average kinetic energy is less at the long delay, the distribution is broader. This could be understood on statistical grounds: since the number of photons absorbed per pulse is low, the fluctuations of charge created in the first vs. the second pulse are significant, directly translating into variations in kinetic energy. Alternatively, at shorter delays, the dissociating molecular ions experience less time gaining KEs on various intermediate potential surfaces that may lead to a broad KE distribution even for the same charge state. Therefore, shorter delays result in a KE distribution of a smaller FWHM.

The objective of this experiment was not to carry out a dynamic experiment but to test that the XRSD instrument works as intended. We verified however that the observed kinetic energies and their change are also in quantitative accord with model predictions of Coulomb explosion. The model used is a point charge Coulomb explosion model, described in detail elsewhere [14]. It uses a few empirical parameters to describe the charge build-up and transfer dynamics. We chose a set of parameters that produced the same kinetic energy (16 eV) in the I^{15+} fragment compared to the experiment. Then modeling with the same parameters produced I^{15+} with 8 eV kinetic energy when the pulse was split into two components with the 200 fs delay. Taking into account the experimental uncertainties, particularly of the pulse length and the portion of pulse energy between the first and second pulses, the simplified model is in reasonable agreement with the experimental results. Our experiment gave a verification that the XRSD device operates as intended and demonstrated that it is a valuable experimental tool for probing into femtosecond scale the dynamics of molecules. We recently re-commissioned this XRSD tool to make it more user friendly regarding spatial and temporal overlap of the two pulses at the interaction region by tabulating the positions of the mirrors.

5.2 Commissioning of the XRSD instrument in the water window wavelength range

The experiment with CH_3I described above was performed at 1600 eV, where as we explained above, iodine absorption dominates over that of carbon. For many applications it is of interest to use the split-and-delay apparatus in the water window (280 - 530 eV). In this wavelength range carbon absorption is significant and a different molecular effect is needed for verifying the spatial overlap between the two x-ray pulses. Below we describe a technique that can be used for this purpose when the x-ray wavelength lies in the water window and utilizing the showcase molecule CO to illustrate spatial overlap determination in the water window.

The cross section for 1s ionization of C between 280 and 530 eV is approximately an order of magnitude larger than the cross section for valence ionization of O and the O 1s ionization channel is closed. The experiment was performed at 400 eV, with ~50 fs long x-ray pulses of the approximate intensity 200 μJ (nominal value) in each pulse. Using a three-layer delay line anode detector (Hexanode by RoentDeck Handels GmbH) capable of momentum-resolved ion-ion coincidence detection, we monitored the yield of different dissociation channels at two time delays, 0 fs and 150 fs. The CO sample was delivered in a pulsed molecular beam with 2.2 bar backing pressure propagating perpendicularly to the direction of the propagation of the x-ray beam. Ion fragments were extracted toward the detector using electric fields perpendicular to both the molecular beam and x-ray beam, with the spectrometer operating in the flat-field regime [11]. The detector permits detection of all three components of the ion fragment momenta [11]. This detection scheme allows for momentum conservation to be used to identify true coincidences.

#262243 Received 1 Apr 2016; revised 16 May 2016; accepted 16 May 2016; published 20 May 2016

The predominant ionization mechanism here is also multiphoton ionization of CO leading to its fragmentation and resulting in highly charged states of the C and O fragments. Figure 7 displays O^{2+} ion fragments detected in coincidence with C^{3+} and C^{2+} ions at 0 fs, Fig. 7(a), and 150 fs delay time between the two x-ray pulses, Fig. 7(b). In each case a sharp diagonal feature formed by the ions satisfying the momentum conservation $\mathbf{p}_{Cn+} + \mathbf{p}_{Om+} \leq \delta$, where $\delta \approx 0$, can be seen on top of a broad feature formed by accidental coincidences. In order to look into the charge sharing between the two fragments, we look at the relative yield of the true coincidences (δ = 11 a.u., 20 a.u., and 65 a.u. in the direction of time of flight, molecular beam and x-ray beam, respectively) in two channels, C^{3+}/O^{2+} and C^{2+}/O^{2+}, plotted in Fig. 7(c) and (d), respectively. The ion yield in each channel was normalized to that of the C^{+}/O^{+} channel. We see that the relative yield of the C^{3+}/O^{2+} channel decreases with time delay, while the relative yield of the C^{2+}/O^{2+} does not change between 0 and 150 fs within the error of the measurement.

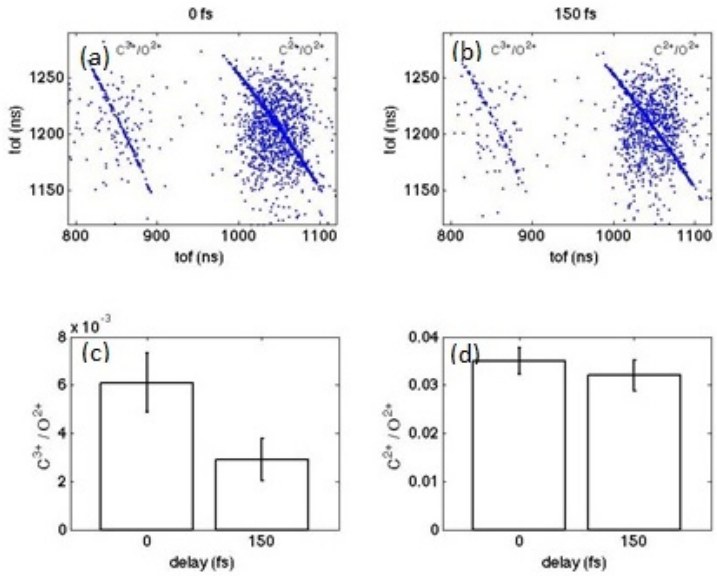

Fig. 7. The yield of O^{2+} ion fragments detected in coincidence with C^{3+} and C^{2+} ions at 0 fs (a) and 150 fs time delay (b), shown as a function of the arrival time of both ions. The yields of the $C^{3+} + O^{2+}$ and $C^{2+} + O^{2+}$ channels, both normalized to that of the C^{+}/O^{+} channel are shown in c and d, respectively.

We explain the observed effect by a dissimilar charge sharing in the states involved in the dissociation paths leading to the two outcomes. We propose that ions detected in the C^{2+}/O^{2+} dissociation channel began their evolution in one of the several bound states of CO^{2+} converging to the C^{+}/O^{+} limit, which are populated via 1s core ionization of the carbon followed by Auger relaxation. When the second x-ray pulse arrives, carbon in CO^{2+} is ionized again and an Auger relaxation leads to the formation of CO^{4+} that dissociates toward the C^{2+}/O^{2+} limit. As the CO^{2+} molecular ion produced by the pump pulse remains bound at 150 fs delay, charge sharing is allowed at both 0 and 150 fs time delay, resulting in similar ion branching ratio at both delay times, as seen in Fig. 7(d). On the other hand, the ions detected in the C^{3+}/O^{2+} channel can originate from several different channels initiated by the pump pulse, some of which involve evolution on repulsive potential energy curves, i.e., dissociative curves. The increase of the internuclear distance leads to dependence of KER on the delay time during which the molecular ions dissociate. The total charge of 5 + can be reached by a shake off in addition to core ionization and the subsequent Auger relaxation. The shake off

#262243 Received 1 Apr 2016; revised 16 May 2016; accepted 16 May 2016; published 20 May 2016

can occur in either of the two ionization steps, but the two cases lead to different outcomes, as we will discuss below. If the shake off accompanies the first ionization step, CO^{3+} is formed as an intermediate charge state. It is known that the dissociation toward the C^{2+}/O^{+} limit is a dominant channel for the dissociation of CO^{3+} compared to that of the C^{+}/O^{2+} limit [11]. Hence, a certain time later CO^{3+} ions dissociate preferentially toward the C^{2+}/O^{+} limit compared with toward the C^{+}/O^{2+} limit. At zero time delay, the two photoionization events occur at similar internuclear distance before the molecular ions break apart. This allows charge sharing between C and O atoms also for both ionization steps by the pump and the probe pulses. At 150 fs only the C^{+}/O^{2+} intermediate step can lead to the formation of the C^{3+}/O^{2+} pair. As C^{+}/O^{2+} intermediate is a minor dissociation channel compared to C^{2+}/O^{+}, the overall effect is a decrease in the yield of the C^{3+}/O^{2+} channel at 150 fs compared to that of the zero time delay, which is visible in Fig. 7(c). When the shake off accompanies the second core ionization step, the intermediary ions begin evolution in one of the bound CO^{2+} states, where charge sharing is possible at either of the time delays considered here. These fragments comprise a time-independent signal in our measurement. This is in agreement with the observation that the yield in the C^{3+}/O^{2+} channel, although diminishes, does not vanish completely at 150 fs.

Dissimilar interatomic charge sharing in different states of molecular ions of CO can thus exhibit distinct time-dependent signatures in yields of different molecular fragmentation channels. With the example of $C^{3+} + O^{2+}$ and $C^{2+} + O^{2+}$ channels, monitored with ion-ion coincident detection, we demonstrated how this effect can be used to verify spatial overlap between the two x-ray pulses with the XRSD instrument [11]. Because the technique can be used below the oxygen K edge, it is well suited for the water window wavelength x-ray range, where significant crystallography and spectroscopy applications are relevant for biology and material sciences.

6. Conclusion and perspectives

We have described the design and operation of a compact, relatively low cost two mirrors x-ray split and delay device for use with the two soft x- ray beamlines (AMO and SXR) at the LCLS [12, 17, 18]. The device splits the incoming FEL pulse with an edge polished mirror, delays the remaining portion of the pulse and recombines them in the interaction region of the experimental end-station. The performance of the instrument was demonstrated in a subsequent experiment [11] to the commissioning of the tool. The XRSD instrument has added x-ray pump/x-ray probe capability at the LCLS allowing a large variety of experiments to be conducted in the future in atomic and molecular science, chemical physics, nanoscience, condensed matter physics and imaging of biological systems.

We foresee that this tool could be built and used at other FEL facilities, especially due to its relative low cost. It could also be expanded to a much wider span of photon energies and delay time with the new generation of x-ray FELs around the world. These tools will be widely available and expanded to be used at any wavelength, any location along the beam, and will become a necessary device for any beamline.

Acknowledgments

This work was funded by the Department of Energy, office of Science, Basic Energy Sciences (BES), Division of Chemical Sciences, Geosciences, and Biosciences under a SISGR program1 No. DE-SC0002004, under grant No. DE-SC0012376 and for the Linac Coherent Light Source (LCLS), SLAC National Accelerator Laboratory, under Contract No. DE-AC02-76SF00515. EK acknowledges the support by the Academy of Finland. LF acknowledges the support by Defense Advanced Research Project Agency Contract 12-63-PULSE-FP014, and by National Nuclear Security Administration Cooperative Agreement DE-NA0002008. We thank Daniele Cocco and Nicholas Kelez from LCLS for their expert advice as well as the LCLS technical staff for their help and dedication.

#262243 Received 1 Apr 2016; revised 16 May 2016; accepted 16 May 2016; published 20 May 2016